Amorphous Metal/Oxide Nanolaminate

E. William Cowell III,[†] Christopher C. Knutson,[‡] John F. Wager,[†] and Douglas A. Keszler*,[‡]

Department of Electrical Engineering and Computer Science, Oregon State University, Corvallis, Oregon 97331-5501, and Department of Chemistry, Oregon State University, Corvallis, Oregon 97331-4003

ABSTRACT Bilayers of sputtered amorphous multicomponent metal films (AMMFs) and solution deposited amorphous oxide films have been reproducibly deposited with varying thicknesses of 20, 25, and 30 nm to form ordered nanolaminates. Interdiffusion is observed at the AMMF-oxide boundary, leading to unique interface chemistries that are dictated by the nature and order of the deposition processes.

KEYWORDS: nanolaminate • thin films • amorphous metal • oxide • XPS • interface

INTRODUCTION

In this letter, we describe a new class of nanolaminates and their unique interfacial characteristics. Nanolaminates in the present context are defined as stacks of alternating ultrathin layers of dissimilar materials. Such laminates have engendered interest for their ultra-low thermal conductivities (1, 2), high-areal capacitance densities (3), and enhanced mechanical properties (4).

They have been fabricated using a variety of techniques. Atomic-layer deposition (ALD) has been used to deposit insulator/insulator (5–7) and insulator/metal systems (8, 9). Pulsed-laser and aqueous-solution deposition have been used to produce high-quality oxide/oxide nanolaminates (10, 11), and DC magnetron sputtering provides a convenient means for deposition of metal/metal systems (4). In this contribution, we outline a new approach relying on the combination of simple DC magnetron sputtering and solution processing for synthesis of very high quality, readily reproduced nanolaminates built from an amorphous metal and an amorphous oxide. Combining these materials at the nanometer scale through the selected deposition methods provides unprecedented opportunities for inducing and studying interlayer chemical reactions and designing unique, chemically graded interfaces.

The oxide component is an alumina-rich phosphate (AlPO) (12) that is readily deposited from an aqueous solution. Through spin coating, film thickness can be precisely controlled by adjusting concentrations of the solution components. Because the aqueous solution contains no organic species, a high-temperature burn out is not required, allowing production of high-quality films at temperatures much lower than those associated with a conventional sol–gel process employing metal-organic precursors. The aqueous solution-based deposition techniques also offer an easily managed method for producing high-quality films with simple beaker chemistries and extremely short processing times.

The Zr–Al–Cu–Ni amorphous multicomponent metal film (AMMF) was first investigated by Sharma and co-workers (13). This alloy, as a bulk material, exhibits superior mechanical strength arising from its amorphous nature. It has also been deposited in thin-film form via magnetron sputtering, yielding an atomically smooth surface (13). This smoothness makes the Zr–Al–Cu–Ni AMMF an especially attractive candidate for incorporation in nanolaminates. One of the driving forces controlling the amorphous nature of an AMMF is the disparate atomic radii among the constituent atomic metal components. If the condition of high disparity is met, a high degree of flexibility in the composition of AMMFs can be achieved. Compositional flexibility creates an ability to tune the work function and to engineer the physical properties of the resulting interface between the AMMF and the solution-derived oxide. Therefore, AMMFs appear to be intriguing materials for use in engineering potential barriers and controlling charge in metal-insulator devices.

We demonstrate below that AlPO/Zr–Al–Cu–Ni interfaces exhibit unique chemical characteristics on the basis of the method of film deposition. The nanolaminate structure is especially well-suited for investigation of these characteristics, as the modulation of interfacial properties can be controlled and then analyzed within a single nanolaminate structure by changing film and bilayer thickness.

RESULTS AND DISCUSSION

The solution precursor for the amorphous oxide used in the nanolaminate was prepared as previously described (12) to a 0.1 M concentration of aluminum. The solution was then spin coated onto the AMMF at a speed of 3000 rpm for a duration of 30 s, followed by treatment at 300 °C for 1 min on a hot plate.

The Zr–Al–Cu–Ni AMMF was deposited by using DC magnetron sputtering at a power of 60 W, a pressure of 3 mTorr, and a 20 sccm flow of Ar (g). The deposition rate at these conditions was measured to be ∼10 nm/min. The
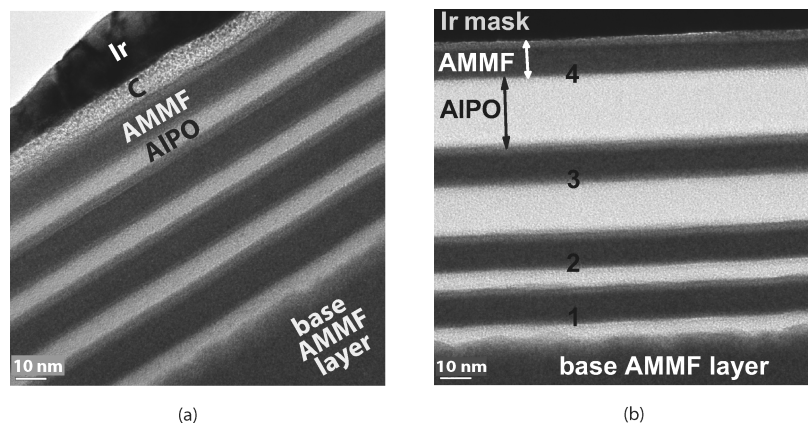
(a)

(b)

FIGURE 1. (a) TEM micrograph of an AlPO/AMMF nanolaminate comprised of four 20 nm AlPO/AMMF bilayers. Carbon and iridium layers are deposited onto the top layer of the AMMF to prevent damage during focused ion beam (FIB) sample preparation. (b) TEM micrograph of an AlPO/AMMF nanolaminate comprised of 4 AlPO/AMMF bilayers. The lower two bilayers have a 20 nm thickness target; the AlPO thickness of bilayers 3 and 4 is targeted at 15 and 20 nm, respectively.

AMMF composition from EPMA analysis of a 200-nm film was established as $Zr_{40}Cu_{35}Al_{15}Ni_{10}$. A base layer for the nanolaminate comprising 200 nm of AMMF was first deposited onto a 25×25 mm^2 substrate of Si coated with 100 nm of thermally grown SiO_2. Electron diffraction from the AMMF layer confirms the amorphous nature of the film.

An initial nanolaminate was fabricated via deposition of eight alternating 10-nm thick films of AlPO and AMMF. Electron scattering through the entire stack reveals no evidence of crystallization. A TEM micrograph of the full nanolaminate consisting of four bilayers, each targeted at a thickness of 20 nm, is shown in Figure 1a. The surface of the base 200 nm AMMF is rather rough, whereas subsequent 10 nm AMMF layers are smooth. The roughening of the thick base layer has been consistently reproduced in subsequent nanolaminates, cf. Figure 1b. To investigate the cause of the roughening, we fabricated a nanolaminate with a 10 nm AMMF layer as the base. A comparison of X-ray reflectivity data between a nanolaminate with a 200 nm base layer and a nanolaminate with a 10 nm base layer indicates that the 10 nm layer is much smoother. The fringes in the XRR pattern collected from the 10 nm base nanolaminate extend 5° 2θ further than the pattern from the 200 nm base nanolaminate, consistent with the roughening of the thicker film. Investigation into the driving force for formation of the 200 nm AMMF roughening is ongoing.

A high-angle annular dark field (HAADF) image of the two bilayers nearest the 200 nm AMMF base layer of the nanolaminate shown in Figure 1a is presented in Figure 2. The contrast of the HAADF image is proportional to the atomic numbers of the constituent elements, and it indicates that the interfacial regions between the AlPO and AMMF layers contain elements lighter than those in the AMMF. The AlPO and AMMF interfaces exhibit contrasts that differ from both the AlPO and the AMMF in the secondary TEM micrograph. The contrast of the interfacial regions between the AlPO and AMMF is similar in appearance to the top of the nanolaminate, which forms on the last-deposited AMMF layer at room temperature in air without heating. Hence, even without heat, the AMMF film exposed to air appears to form a native
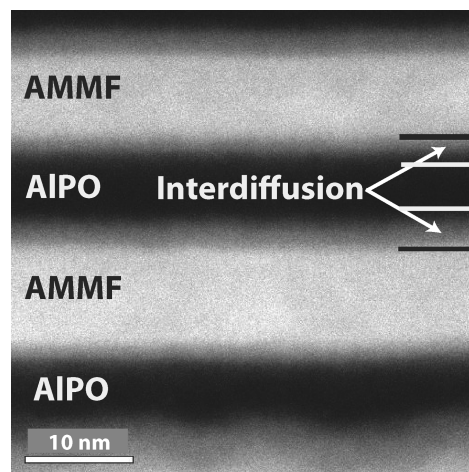

FIGURE 2. HAADF image of lower 2 bilayers. Distances between horizontal lines are 10 nm based on image scale. Interdiffusion layers are hypothesized as metal atoms from AMMF diffusing into AlPO.

oxide coating. This assertion is supported by XPS depth profiling, vide infra, where Zr(IV) is observed on top of the final AMMF layer in the nanolaminate. Interestingly, the thickness of this native overcoat is similar to the thicknesses of the AMMF/AlPO interfaces on the top sides of the AMMFs. These observations are again consistent with the formation of a native oxide on exposing the AMMF to air with the result that the AlPO is likely being solution-deposited onto an oxide-coated AMMF.

EDS analysis was performed on the TEM sample to investigate elemental composition across the AMMF/AlPO interfaces. The EDS analysis showed that Cu and Zr atoms diffuse deeply into the AlPO layer, whereas the Ni atoms are substantially retained in the AMMF. The veracity of these results, however, was initially uncertain because of possible beam spreading of the incident electrons through the TEM sample, causing only an apparent presence of Zr and Cu in the AlPO film. Simulations of the beam spread, performed by the Analytical and Development Labs (ADL) at Hewlett Packard-Corvallis were consistent with an areal resolution of the EDS signal on the order of the dimension of the AlPO film. The simulations supported the view that the Zr and Cu EDS signals in the AlPO
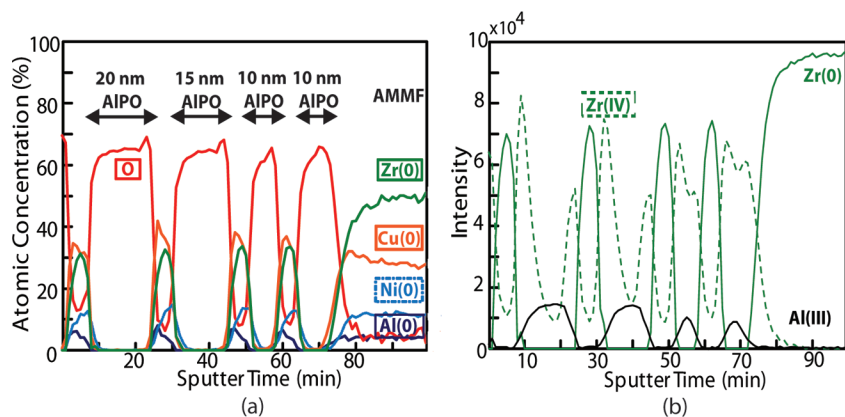
FIGURE 3. (a) XPS depth profile of Zr, O, Cu, Al, and Ni taken through the nanolaminate shown in Figure 1b. (b) XPS depth profile of Zr(IV) and Al(III) taken through the nanolaminate shown in Figure 1b.

film could be an artifact of beam spreading through the sample. Applying the simulations to possible signal blurring, however, was inconsistent with the Ni signal, which appears to go to zero in the AlPO film. This inconsistency in the Ni signal did not support a beam-spreading hypothesis.

A depth profile using X-ray photoelectron spectroscopy was undertaken to further investigate the composition of the nanolaminate layers and to examine the possible beam-spreading effects of the EDS analysis. The profile data shown in Figure 3 were taken from the nanolaminate shown in Figure 1b, where the AlPO layers were deposited at thicknesses of 20, 15, and 10 nm. As seen in Figure 3a, the general characteristics of the laminated structure are compositionally verified. Layers of AMMF and AlPO are clearly evident, and the layer thicknesses of AlPO, ranging from 10 to 20 nm, are confirmed. More detailed profiles for Zr(0), Zr(IV), and Al(III) are summarized in Figure 3b. Here, the presence of Zr(0) in the AMMF is confirmed. In the AlPO layers, however, the oxidation state is Zr(IV). For the 10 nm AlPO films, the Zr(IV) signal reveals that Zr has permeated the entire thickness. For the thicker 15 and 20 nm AlPO films, there is a bifurcation in the Zr signals, indicating that the AlPO layers are sufficiently thick to inhibit Zr migration. The Cu, Zr, and Ni metal profiles, presented in Figure 3a, show that the metal signals do not exist through the AlPO, and that the atomic concentrations of the Cu and Ni metals match those of the bulk. No signals were detected for Cu(II) or Ni(II), indicating that the oxidation−reduction reaction between the AMMF and AlPO is selective to Zr. The lack of XPS metal signals in the AlPO suggests that the Cu EDS signal in the AlPO is an artifact of beam spreading or signal averaging and that the Zr signal was in fact Zr(IV).

As seen in Figure 3b, the Zr(IV) XPS profiles differ for the top and bottom interfaces in the nanolaminate structure. The higher intensity Zr(IV) peak repeatedly occurs at the interface involving sputter deposition of the AMMF onto the AlPO, whereas the lower intensity Zr(IV) peak occurs for deposition of AlPO onto the AMMF. Clearly, the degree of Zr oxidation is finely controlled, in part, by the deposition technique. A detailed discussion of the oxidation-reduction chemistry and the resulting interface structure are beyond the scope of the current contribution; they will be addressed in forthcoming publications. Presently, the creation of divergent interfaces in a laminate structure represents a unique lever for controlling characteristics on the small-end of the nanometer scale. Such control provides new avenues for tailoring interfaces and developing the potential of nanoscale electronic devices built from simple metal-insulator materials sets (14).

REFERENCES AND NOTES

(1) Costescu, R. M.; Cahill, D.; Fabreguette, F.; Sechrist, Z.; George, S. *Science* **2004**, *303*, 989−990.
(2) Chiritescu, C.; Cahill, D.; Nguyen, N.; Johnson, D.; Bodapati, A.; Keblinski, P.; Zschack, P. *Science* **2007**, *315*, 351−353.
(3) Brennecka, G.; Parish, C.; Tuttle, B.; Brewer, L. *J. Mater. Res.* **2008**, *23*, 176−181.
(4) Wang, Y.; Li, J.; Hamza, A. V.; Barbee, T. W. *Proc. Natl. Acad. Sci. U.S.A.* **2007**, *104*, 11155−11160.
(5) Elam, J. W.; Sechrist, Z. A.; George, S. M. *Thin Solid Films* **2002**, *414*, 43−55.
(6) Cho, M.-H.; Roh, Y. S.; Whang, C. N.; Jeong, K.; Choi, H. J.; Nam, S. W.; Ko, D.-H.; Lee, J. H.; Lee, N. I.; Fujihara, K. *Appl. Phys. Lett.* **2002**, *81*, 1071−1073.
(7) Leskelä, M.; Kemell, M.; Kukli, K.; Pore, V.; Santala, E.; Ritala, M.; Lu, J. *Mater. Sci. Eng., C* **2007**, *27*, 1504−1508.
(8) Sechrist, Z. A.; Fabreguette, F. H.; Heintz, O.; Phung, T. M.; Johnson, D. C.; George, S. M. *Chem. Mater.* **2005**, *17*, 3475−3485.
(9) Grubbs, R. K.; Nelson, C. E.; Steinmetz, N. J.; George, S. M. *Thin Solid Films* **2004**, *467*, 16−27.
(10) Karakaya, K.; Barcones, B.; Rittersma, Z.; van Berkum, J.; Verheijen, M.; Rijnders, G.; Blank, D. *Mater. Sci. Semicond. Process.* **2006**, *9*, 1061−1064.
(11) Anderson, J.; Munsee, C.; Hung, C.; Herman, T. P. G.; Johnson, D.; Wager, J.; Keszler, D. *Adv. Funct. Mater.* **2007**, *17*, 2117−2124.
(12) Meyers, S.; Anderson, J.; Hong, D.; Hung, C.; Wager, J.; Keszler, D. *Chem. Mater.* **2007**, *19*, 4023−4029.
(13) Sharma, P.; Zhang, W.; Amiya, K.; Kimura, H.; Inoue, A. *J. Nanosci. Nanotechnol.* **2005**, *5*, 420−424.
(14) Reuss, R.; Chalamala, B.; Moussessian, A.; Kane, M.; Kumar, A.; Zhang, D.; Rogers, J.; Hatalis, M.; Temple, D.; Moddel, G.; Eliasson, B.; Estes, M.; Kunze, J.; Handy, E.; Harmon, E. *Proc. IEEE* **2005**, *93*, 1239−1256.

AM100283M